Electroosmotic Pumps Fabricated From Porous Silicon Membranes

Shuhuai Yao, Alan M. Myers, Jonathan D. Posner, Klint A. Rose, and Juan G. Santiago, *Member, IEEE, Member, ASME*

***Abstract*—N-type porous silicon can be used to realize electroosmotic pumps with high flow rates per applied potential difference. The porosity and pore size of porous silicon membranes can be tuned, the pore geometry has near-unity tortuosity, and membranes can be made thin and with integrated support structures. The size of hexagonally packed pores is modified by low-pressure chemical vapor deposition (LPCVD) polysilicon deposition, followed by wet oxidation of the polysilicon layer, resulting in a pore radius varying from 1 to 3 μm. Pumping performance of these devices is experimentally studied as a function of pore size and compared with theory. These 350-μm-thick silicon membranes exhibit a maximum flow rate per applied field of 0.13 ml/min/cm^2/V. This figure of merit is five times larger than previously demonstrated porous glass EO pumps. [1494]**

***Index Terms*—Electroosmotic pump, porous silicon membrane, zeta potential.**

I. Nomenclature

A	Cross-sectional area (m^2).
L	Length (m).
I	Current (A).
P	Pressure capacity (Pa).
Q	Flow rate (ml/min).
V	Voltage (V).
a	Pore radius (m).
$c.$	Electrolyte ionic concentration (M).
c_o	Reference electrolyte ionic concentration (M).
d	Center-to-center distance (m).
ε	Permittivity of liquid (F/m).
μ	Viscosity (Pa s).
μ_p	Mean value of intensity peak (-).
σ	Electrolyte conductivity (S/m).
σ_p	Standard deviation of intensity peak (-).
ζ	Zeta potential (V).
ζ_o	Reference zeta potential for c_o (V).
ν	Pore density (-).
γ	Relative pore density, $\gamma = \#\text{open}/\#\text{ideal}$ (-).
ψ	Porosity, $\psi = \gamma\psi_o$ (-).
ψ_o	ideal porosity (-).
τ	Tortuosity (-).

Subscripts

eff	Effective value.
max	Maximum value.

Manuscript received January 4, 2005; revised October 28, 2005. This work is supported by Intel Corporation. Work was performed in part at the Stanford Nanofabrication Facility (a member of the National Nanotechnology Infrastructure Network), which is supported by the National Science Foundation under Grant ECS-9731294. Subject Editor F. K. Forster.

S. Yao, J. D. Posner, and K. A. Rose are also with the Department of Mechanical Engineering, Stanford University, Stanford, CA 94305 USA.

A. M. Myers is with the Intel Corporation, Santa Clara, CA 95052 USA.

J. G. Santiago is with the Department of Mechanical Engineering, Stanford University, Stanford, CA 94305 USA (e-mail: juan.santiago@stanford.edu).

Digital Object Identifier 10.1109/JMEMS.2006.876796

II. Introduction

ELECTROOSMOTIC (EO) pumps have no moving parts and are capable of generating high-flow rate per device volume. These devices have significant pressure capacity in a compact structure and use direct current potential differences of tens to hundreds of volts. They therefore offer some advantages over other miniature pumps for microchannel cooling applications [1] and integrated bioanalytical systems [2]–[4]. Packed-column EO pumps have been fabricated by packing and sintering 1–20 μm silica and borosilicate glass particles [5]–[11]. In parallel efforts, Chen and Santiago [12] and Laser *et al.* [13] demonstrated EO pumps fabricated using planar micromachined structures in glass and silicon substrates. Takamura *et al.* [14] developed a ten-stage cascaded EO pump on a quartz plate. EO pumps have also been fabricated using commercially available porous glass frits (e.g., from Robu Glasfilter-Geräte GmbH, Germany). These glass filters, or "frits", are typically 40 mm in diameter, 1–5 mm thick, with mean pore diameters of 1 to 2 μm, porosities of 0.2 to 0.35, and tortuosities of 1.4. The pumping flow rate and pressure capacity of such pumps are limited by morphology (e.g., quantified in terms of tortuosity), the ability to reproducibly fabricate submicron pore diameters, and structural strength [15]. Laser and Santiago [4] presented a review of miniature pumps including comparisons of EO pumps to other miniature pump technologies.

Porous silicon has attracted increasing interest in a wide spectrum of potential applications, including silicon quantum wire and fuel cell membranes [16]–[18]. A porous silicon membrane consists of a dense array of straight, nearly-cylindrical pores. Pore diameter distributions are very narrow, and aspect ratios as high as 250 are possible [19]. In this work we explore EO pumps that use porous silicon membranes as pumping media. Porous silicon structures were modified with a suitable thin film deposition, including thermal oxide or oxidized low-pressure chemical vapor deposition (LPCVD) polysilicon, to provide reliable insulation surfaces. The effects of pore size and porosity on flow rate and pressure were demonstrated using experiments from eight samples with varying pore radius. The results were compared to the electroosmotic pumping theory. The repeatability and stability of pump operation were studied for various working solutions. Some design issues of the membrane dimensions and the electrode placement are discussed for the optimization of pump performance. These structures have an advantage over porous glass frits in that the porous silicon tortuosity approaches unity.

1057-7157/$20.00 © 2006 IEEE

Silicon fabrication also offers control of porous structure thickness, pore radius, and porosity.

III. Theory of Electroosmotic Pumping

We have modeled EO pumping in porous materials by treating the media as an array of cylindrical microchannels of uniform pore radius a, with tortuosity τ, and porosity ψ. Flow rate dependence on applied voltage and pressure can then be described as [20]

$$Q = \frac{\psi}{\tau}\left[-\frac{\mathrm{PA}a^2}{8\mu L} - \frac{\varepsilon\zeta \mathrm{AV_{eff}}}{\mu L} f\right] \tag{1}$$

where

$$f = \int_0^a \left(1 - \frac{\varphi}{\zeta}\right)\frac{2r}{a^2}dr. \tag{2}$$

The solution to the integral can be obtained by solving the Poisson-Bolzmann equation for electrical potential in the channel [20], [21]. The model can easily (and more exactly) be applied to porous silicon membranes with $\tau = 1$. The maximum flow rate, current, and pressure are as follows [15]:

$$Q_{\max} = -\psi A\varepsilon\zeta V_{\mathrm{eff}} f/(\mu L) \tag{3}$$

$$I_{\max} = \psi A\sigma V_{\mathrm{eff}} f/(Lg) \tag{4}$$

$$P_{\max} = -8\varepsilon\zeta V_{\mathrm{eff}} f/a^2 \tag{5}$$

where ζ is the zeta potential and g is a dimensionless flow rate per current ratio. The parameters f and g both tend to unity for large pore to Debye length, λ, ratios [21]. A detailed numerical calculation and analytical, approximate expression for g in cylindrical coordinates have been presented in our previous work [20]. These equations allow the prediction of the performance for an EO pump, given pore radius, zeta potential, macroscopic dimensions of the pumping media, and working fluid chemistry.

The ratio of the maximum flow rate to the maximum achievable pressure of an EO pump, $Q_{\max}/P_{\max}$, can be expressed as

$$Q_{\max}/P_{\max} = \psi A a^2/(8\mu L) \tag{6}$$

Combining (3) and (4), we can also derive an analytical expression for the maximum flow rate to maximum current ratio

$$Q_{\max}/I_{\max} = -\varepsilon\zeta g/(\mu\sigma). \tag{7}$$

A model for the zeta potential as a function of pH and concentration has been presented [22], [23]. The zeta potential is strongly dependent on the pH of the solution, and is weakly dependent on the ionic strength. We use measurements of $Q_{\max}/I_{\max}$ to investigate the zeta potential of porous silicon membranes at various electrolyte conditions and compare with this model.

The thermodynamic efficiency of an EO pump can be expressed as $2V_{\mathrm{eff}}\varepsilon^2\zeta^2 fg/(V_{\mathrm{app}}\mu\sigma a^2)$ [20]. This relation and (7) highlight an advantage and disadvantage of the current EO pumps. For applications where high flow rate per power, $Q/(I * V_{\mathrm{app}})$, is required (e.g., using the working fluid as a carrier of heat but pumping against low pressure loads), we find that relatively large pores are favorable as low conductivity, σ, working electrolytes can be used and still maintain g near unity. Note that the thin dimensions of porous silicon pumps also lower V_{app} for a given Q. On the other hand, for applications requiring high-pressure work, QP, there is an optimum pore diameter that maximizes the ratio fg/a^2. As we shall see below, the current pumps have excellent flow per power performance (typically four times better than porous glass pump), but relatively low thermodynamic efficiency (e.g., 0.05% versus 0.2% for glass pumps with 1.1 μm diameter pores) [15]. Yao and Santiago [20] and Reichmuth *et al.* [24] discuss optimization of EO pump thermodynamic efficiency.

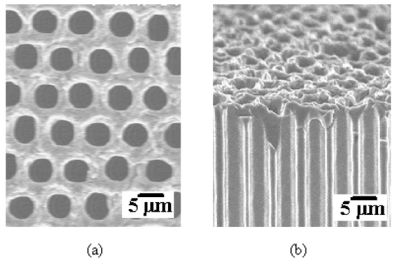

Fig. 1. SEM of porous silicon structure. The sample (obtained from Neah Power Systems, Inc. Bothell, WA) has a thermally grown SiO_2 film approximately 0.25 μm thick. (a) Top view showing a hexagonal array of pores with diameters on the order of 6 μm and pitch distances of 8.5 μm. (b) Cross-sectional view showing straight pores with a uniform, conformal surface layer.

IV. Materials and Fabrication

In this section, we describe and characterize porous silicon membranes and the fabrication process.

A. Materials

Porous silicon membranes fabricated from n-type silicon were provided by Neah Power Systems, Inc. (Bothell, WA) for our study. These 350-μm-thick membranes have a hexagonal array of uniform pores with a tortuosity approaching unity. The ideal porosity is determined by the hexagon layout and feature dimensions as

$$\psi_o = 2\pi a^2/(\sqrt{3}d^2) \tag{8}$$

where a is the pore radius and d is the center-to-center distance of pores. Fig. 1 shows scanning electron microscope (SEM) images of top and cross-sectional view of porous silicon membranes. The top view shows the membrane's hexagonal array of pores with diameters on the order of 6 μm, and center-to-center distances of 8.5 μm. The nominal porosity of these structures is 0.45. The cross-sectional SEM shows straight, nearly uniform diameter pores.

B. Fabrication

The porous silicon membranes were fabricated as an array of samples in a four inch diameter silicon wafer. The as-received samples were first diced on a wafer saw in order to obtain individual 2×2 cm membranes dies with centered 1 cm^2 porous regions. The membranes were then cleaned in a solution mixture of 5:1 sulfuric acid (J. T. Baker, Phillipsburg, NJ) and 30%

TABLE I
CHARACTERIZATION DATA OF THE 1 cm × 1 cm POROUS SILICON MEMBRANES.

	L (μm)	γ	a (μm)		ψ	
			SEM	Q_{max}/P_{max}	SEM	Q_{max}/P_{max}
Native SiO_2	370	0.95	2.9±0.21	3.2	0.39	0.48
0.25 μm poly + SiO_2	374	0.98	2.5±0.10	2.8	0.30	0.38
0.5 μm poly + SiO_2	351	0.95	1.8±0.23	2.2	0.15	0.23
1.0 μm poly + SiO_2	349	0.88	1.7±0.17	1.8	0.13	0.14
1.25 μm poly + SiO_2	348	1.0	1.2±0.18	1.3	0.067	0.083
1.5 μm poly + SiO_2	348	1.0	1.1±0.12	1.2	0.062	0.071
1.75 μm poly + SiO_2	346	1.0	1.0±0.19	1.0	0.051	0.049
2.0 μm poly + SiO_2	348	0.95	0.86±0.18	0.92	0.034	0.039
High density native SiO_2	373	0.87	2.0±0.09	2.2	0.42	0.50

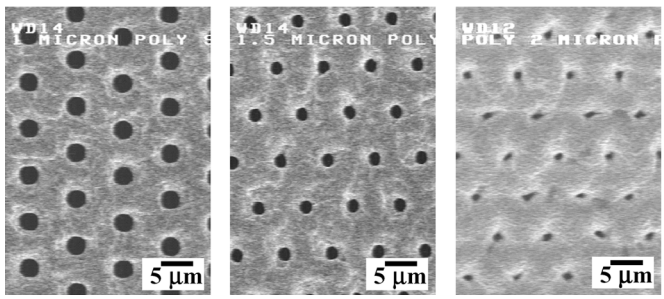

Fig. 2. Top view SEM's of porous silicon structures with polysilicon deposition thicknesses of 1 μm, 1.5 μm, and 2 μm (respectively from left to right). These polysilicon layers were wet oxidized to achieve 0.25 μm SiO_2 coating surfaces.

hydrogen peroxide (J. T. Baker, Phillipsburg, NJ) for 20 minutes. This was followed by a dip in a 5:1:1 mixture of deionized water, hydrochloric acid (J. T. Baker, Phillipsburg, NJ), and 30% hydrogen peroxide. The final cleaning step involved a dip in a 50:1 solution of hydrofluoric acid and 30% hydrogen peroxide. Next, the silicon structures were modified with a suitable thin film deposition, including either thermal oxide (SiO_2) or oxidized LPCVD polysilicon. The liner materials on the silicon substrate provide reliable electrical insulation for operation. The SiO_2 coating also improves the surface charge density and operation stability of the pump. LPCVD polysilicon deposition, followed by wet oxidation of the polysilicon layer, was used to increase the coating thickness and to provide control of the pore diameter. Polysilicon deposition was performed at 620°C in a silane/hydrogen environment. In this study, we tried LPCVD polysilicon deposition for 0.3 to 2.5 h, resulting in polysilicon deposition thickness varying from 0.25 to 2 μm. A list of the fabricated samples is given in Table I. All wet oxidations were performed for two hours at 900 °C. The wet oxidations were preceded and followed by 10 min dry oxidations. Initial sample oxidation with no polysilicon layer present resulted in warped membranes, and this warpage increased in severity with oxidation time and temperature. Fig. 2 shows a top down SEM view of the porous silicon structures with polysilicon deposition thickness of 1 μm, 1.5 μm, and 2 μm. The porous silicon membranes were modified to various pore sizes with oxidized LPCVD polysilicon deposition. All of the polysilicon layers in these images were wet oxidized to have a 0.25-μm SiO_2 surface layer.

V. POROUS SILICON CHARACTERIZATION

In this section we present sample measurements of feature dimensions and pore density of the hexagonal porous silicon structures using image analysis. Pore size distributions were determined from multiple scanning electron microscopy images; and pore density was determined from optical microscopy images.

A. Pore Size Analysis

We used analysis of scanning electron microscope (SEM) images to measure the average pore size a of samples with eight polysilicon layer thicknesses. SEM images (with 640×480 pixels of view 75×56 μm) were taken at the center and four corners of each sample as local representative samples across the membrane surface. Top view SEM images were used for image analysis. To characterize the effective pore diameter, we assume uniform pores along the length of the pore. We analyzed the cross sections (e.g., see Fig. 1(b)) of two samples in detail (we examined other samples in less detail) and found pore diameter typically varied less than about 10% along the length of the pore. We therefore neglected such nonuniformity in these very high aspect ratio (350:6 or higher) pores. The flow chart in Fig. 3 summarizes the segmentation scheme used to analyze the images. The contrast between dark pore regions to light polysilicon regions was used to binarize the grayscale SEM images. As shown in Fig. 4, the intensity histogram of the porous silicon SEM images has a distinct bimodal distribution.

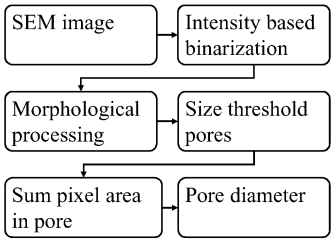

Fig. 3. Pore segmentation algorithm. Grayscale SEM images are converted to black and white using an intensity based binarization scheme to differentiate between dark pores and the lighter surrounding regions. The connected regions of dark pixels are eroded and dilated with a 3 by 3 pixel diamond shaped structuring element to remove spurious dark pixels. Application of a user-specified size threshold to the remaining connected regions eliminates unlikely pore regions. The area of each pore is found by summing the area of pixels within the connected region "pore" regions. Pore diameter was estimated as the diameter of a circle of area equal to the measured pore area.

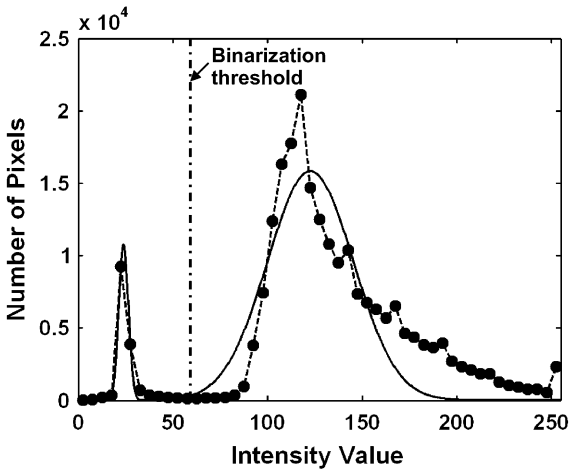

Fig. 4. Pixel intensity histogram from an SEM image of multiple pores. The bimodal distribution in intensity is due to the contrast of the dark pores to the light substrate surface. The binarization threshold is chosen by fitting a two peak gaussian curve to this distribution and selecting a threshold value between the peaks. The threshold value is shown in the plot as a vertical dashed line.

A curve consisting of two summed Gaussian functions was fit to this distribution to approximately characterize the mean intensity and standard deviation of each peak. The binarization threshold was selected as the intensity value at $\mu_p + 2\sigma_p$, where μ_p and σ_p are the mean and standard deviation of the low intensity peak. After binarization, the agglomerated regions of dark pixels were eroded and dilated with a three by three pixel structuring element (with pixel values at four corners set to zero and other pixel values set to unity) to remove spurious dark pixels. This morphological processing element is often called a "diamond shaped" element in signal processing literature [25]. This preliminary process falsely identifies some small, low-intensity regions as pores. This false identification was mitigated by using a user-specified minimum size threshold on pore diameter (typically three standard deviations from the resulting, measured mean pore diameter). The average center-to-center distance of the pores was measured as 8.6 ± 0.026 μm. The area of each pore was then found by summing the number of pixels within each identified pore region. Pore diameter was estimated as the diameter of a circle of area equal to the measured area of each pore. Pore radii resulting from analysis of SEM images are shown in Table I and labeled as "SEM."

B. Pore Density Correction

We found that as many as 13% of the pores in some of our samples were not opened during the porous silicon fabrication process. We used analysis of optical microscopy images to measure the number of open pores for each sample. We used transmitted light mode microscopy for samples with polysilicon deposition layers smaller than of 1.5 μm and fluorescence imaging for smaller pores. In both cases, a TE300 Nikon microscope (Nikon, Japan) fitted with a 10x objective with a numerical aperture of 0.45 (Nikon, Japan), and a cooled CCD camera (Cascade 512, Photometrics, Tucson, AZ) were used. A representative optical image is shown in Fig. 5(a). The color of the transmitted light through the samples varied from white (native samples) to purple (1.25 μm poly) due to spectral filtering due to diffraction. For samples with a polysilicon layer thicker than 1.5 μm, no detectable light was transmitted through the samples in the visible spectrum so we measured the pore density using fluorescence. For these images, we wicked 10 mM rhodamine B dye solution into the pores and imaged in epifluorescence mode.

For the pore density measurements, we obtained 25 representatives images evenly distributed throughout the surface of each sample. Each image spanned an area of 5.73e5 μm^2. Imaged regions were centered within each section of a 25-square Cartesian grid that divided the sample surface. We found 25 sub-image samples provided an accurate measure of open pore density for the entire membrane surface (i.e., increasing sample number by factor of four had a negligible effect on statistical moments).

We determined the total number of open pores per area, ν, using a custom image processing algorithm. Each image was binarized with a user-specified threshold, and the total number of pores was counted with a method similar to that described in Fig. 3. The value of the threshold, which varies from zero to unity, determined the pore/silicon interface and number of pores. Fig. 5(b) shows a plot of the measured pore density as function of the threshold value. The data shows that measured pore density is insensitive to the user-specified threshold value. We used a nominal threshold value of 0.5.

We introduced γ as a correction factor for the ideal porosity ψ_o (i.e., assuming all pores are open), based on the hexagonally packed pore geometry and pore size given in (8). The corrected porosity is defined as $\psi = \gamma\psi_o$. γ is the ratio of the measured pore density ν, and the ideal hexagonally packed pore density of $2/(\sqrt{3}d^2)$ (where d is the average center-to-center distance d measured using the SEM image analysis described above). Measured γ values for nine porous silicon samples are shown in Table I. Combined with (8), actual sample porosity can be simplified as

$$\psi = \nu\pi a^2 \tag{9}$$

As a comparison, we compared these values of ψ to the direct estimates of pore-to-closed-silicon area ratios determined from the SEM image analysis. In all cases, the results of these two

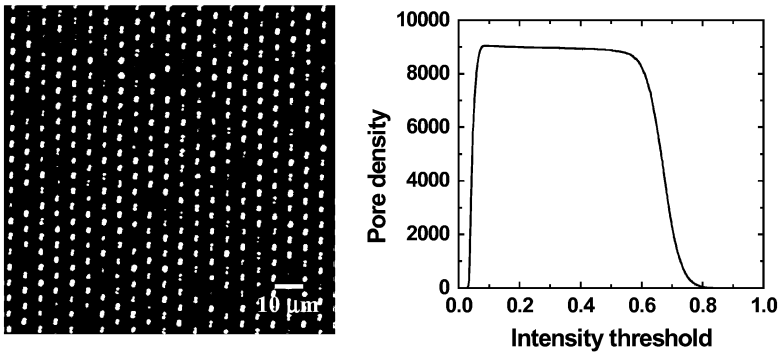

Fig. 5. One the left is a representative optical image of porous silicon using transmission microscopy (left) with a $40\times$ microscope objective $(\mathrm{NA} = 0.45)$. The open pore density of silicon samples was measured using an image processing algorithm applied to these optical images. The figure (on the right) shows measured pore density as a function of the binarization threshold, the only user-specified parameter of the pore measurement algorithm. The algorithm is insensitive to the threshold value.

methods agree to within 5%. The porosity measurements resulting from the SEM image analysis are also listed in Table I, labeled as "SEM".

As further validation of the porosity measurement, we also estimated pore radius of the native-oxide material using measurements of flow resistance (with no applied field). This process gives us a measurement of the ratio Q/P and, from $Q = \nu A \pi a^4 P/L/(8\mu)$, and (9), we can obtain estimates of porosity and pore radius. This yielded values of 0.42 and 3.0 μm, which can be compared to the values of 0.39 and 2.9 μm, respectively, from the image analysis.

VI. Experimental Setup

The pump assembly and the experimental setup for characterizing pump performance were similar to the system described in our previous work [15]. A schematic of the pump assembly is shown in Fig. 6(a). The porous silicon membrane was potted into an acrylic frame using epoxy. The acrylic frame was fabricated using a laser engraving and cutting system (Universal Laser Systems, Scottsdale, AZ), and sandwiched between two halves of a machined acrylic housing. Stainless steel tubulations (Scanivalve Corporation, Liberty Lake, WA) were used for fluidic connection. Platinum wire electrodes wound into a spiral with a spacing of about 3 mm between coils were placed approximately 1 mm from the surfaces of the membrane to provide a roughly uniform electric field. In each experiment, the porous silicon structures were cleaned using 100 mM NaOH and rinsed with deionized water. The structures were then cleaned in an ultrasonic bath (Fisher Scientific, Hanover Park, IL) with deionized water for 20 min.

Fig. 6(b) shows an experimental setup for pump performance characterization with extended capability for varying back pressure. This setup allows for the measurement of the full pressure capacity of the pump in flowing conditions. The back pressure is varied by changing the hydraulic head of a downstream reservoir. This configuration allows us to achieve flow rate measurements under the condition where the maximum adverse pressure difference across the pump exceeds the maximum pump source pressure (resulting in negative flow rates). We can also apply favorable pressure differences across the pump. Pressure is measured downstream of the pump using a pressure transducer (OMEGA, Stamford, CT). Flow rate is measured using a balance (ACCULAB, Newtown, PA) upstream of the pump.

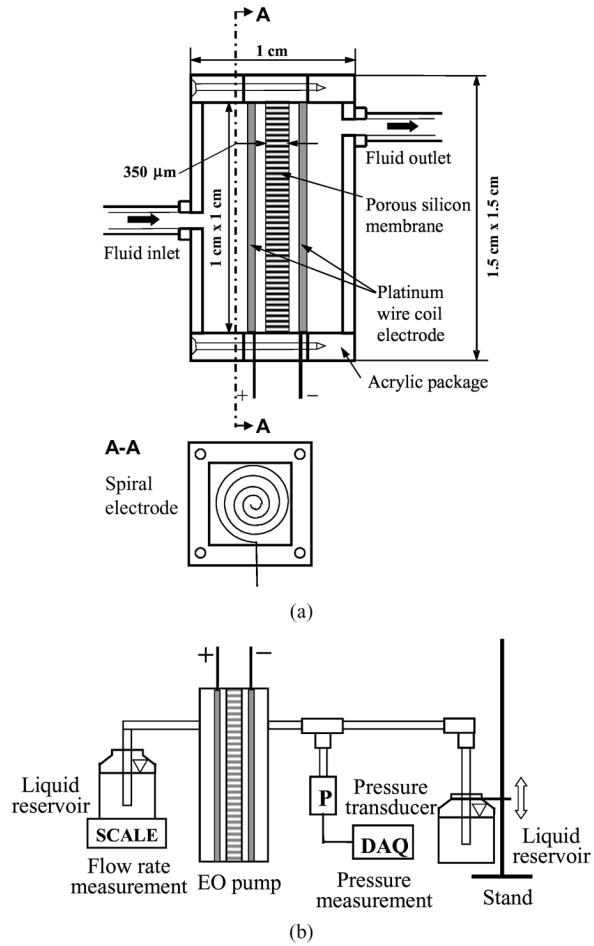

Fig. 6. (a) Schematic of porous silicon EO pump assembly and the spiral electrode configuration. (b) Schematic of setup for pump characterization with extended capability for varying back pressure. The back pressure is changed by varying the height of the hydraulic head of one reservoir using the stand on the right.

VII. Results and Discussion

We first demonstrate a representative experiment in which the dielectric breakdown strength of the pumps was exceeded. We

then present a quantification of pump performance in the form of flow rate, current, and pressure results, and compared these with model predictions. We also discuss the repeatability of pump operation. The zeta potential of the porous silicon membranes is then characterized as a function of the ionic molar concentration. Finally, we discuss design criteria for porous silicon EO pumps in terms of membrane geometry and device design.

A. Electrical Breakdown

The dielectric breakdown strength of the porous-silicon EO pumps was determined for an oxide/porous-silicon sample. For this destructive test, EO pump current was monitored as a function of increasing applied potential difference. We define the dielectric strength of the membrane coatings as the applied potential at which the current increases dramatically. A representative measurement of EO pump current as a function of the applied voltage is shown in Fig. 7. This porous silicon membrane sample was wet oxidized at 900 °C for two hours, with an accompanying 10 minute dry oxidation both preceding and following the wet oxidation. The estimated oxide film thickness is 0.25 μm. The data of Fig. 7 demonstrates that the SiO_2 surface layer provided reliable insulation for operation at up to approximately 400 V. The data point labeled with an "x" was the first current measurement immediately after breakdown. Before breakdown, the electric current was directly proportional to applied voltage with a resistance was 10 000 Ohms. This electrical resistance is the sum of the membrane resistance and the two resistances that account for the spacing between the electrodes and the membrane surfaces [15]. In a subsequent experiment performed after breakdown, the system resistance was reduced by a factor of 2.5 and the current showed a slightly nonlinear increase with the voltage. The dielectric breakdown of n-type silicon coated with thermal oxide and LPCVD nitride films in aqueous solution has been studied by Harrison *et al.* [26]. Our estimated breakdown electrical field of 0.25 μm thermal oxide coated silicon, 1e9 V/m, showed reasonable agreement with their measurements, 8e8 V/m.

B. Flow Rate and Pressure Performance

Eight porous silicon membranes with varying pore size were tested. The maximum pore diameter sample had a native oxide surface and the rest had various thicknesses of polysilicon deposition followed by wet oxidation.

As discussed by Yao *et al.* [15], the effective voltage across the pump is a function of the device overpotential and the resistances associated with electrode-to-pump spacing. We estimate these values from a preliminary calibration experiment. We treat the pump system as three resistors (spacing-membrane-spacing) in series. The Ohmic resistance per area of the electrode spacing can be approximated as a function of the conductivity of the solution and the spacing from the electrode to the membrane surface. Both overpotential and electrode spacing can then be determined from the measured current versus voltage response of the pump. Extrapolation of the Ohmic regime of current versus voltage to the zero current point provides the system overpotential. Electrode spacing is estimated from this value and the total system resistance. The average overpotential values and the electrode-membrane spacings were respectively 2.1 ± 0.9 V and 1.0 ± 0.3 mm; these values were used to calculate effective voltage and to predict the pump performance [15].

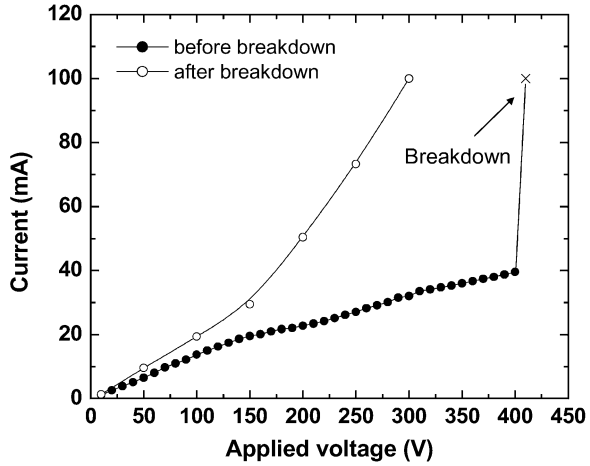

Fig. 7. Porous silicon EO pump current versus applied voltage from 0 to 410 V (dark symbols) at 10 V intervals. Electrical breakdown occurred between 400 and 410 V. Before breakdown, the electric current is proportional to the applied voltage and the resistance is relatively high. After breakdown (open symbols), the system resistance is reduced by a factor of 2.5.

For pump performance characterization measurements, a simpler experimental setup was used in which the moveable reservoir on the cathode side in Fig. 6(b) was replaced with a clear tube. Tracking of a meniscus in this tube provided a method of measuring flow rate. The velocity of the liquid/gas interface is used to calculate the bulk velocity of the flow driven by the EO pump. We calibrated this measurement of flow rate using a high-precision syringe pump (Harvard PHD 2000, Harvard Apparatus, Holliston, MA). A micrometering control valve (Upchurch Scientific, Oak Harbor, WA) was integrated downstream of the pump to set desired back pressure. The working electrolyte for the flow rate and pressure data presented here was a 1.0 mM (Na+) sodium borate buffer solution ($Na_2B_4O_7$) with pH 9.2 and an ionic conductivity of 81e–3 S/m. Conductivity and pH were measured using a dual conductivity and pH meter (Corning Pinnacle 542, Cole-Parmer, Vernon Hills, IL).

The maximum pump flow rate, $Q_{\max}$, maximum pump current, $I_{\max}$, and maximum pump pressure, $P_{\max}$, were measured at applied voltages of 10 to 100 V. Note $P_{\max}$ is by definition the pressure generated by the pump at the condition of zero net flow rate. To measure this, we adjusted the height of the downstream reservoir shown in Fig. 6(b) until the flow rate through the system was zero. Fig. 8 shows the expected linear dependence of $Q_{\max}, I_{\max}$, and $P_{\max}$ with effective voltage for the eight porous silicon EO pump devices. Shown together with the data are model predictions for $Q_{\max}, I_{\max}$, and $P_{\max}$ using (3)–(5), and a measured zeta potential value of -104 ± 5 mV (discussed below). The porosity, ψ, and pore radii, a, used in these predictions are those obtained from the image analyzes described above (see Table II). The coefficients f and g were calculated by the numerical model described in [20], a method applicable to these pore geometries. The effective voltage, V_{eff}, was determined using applied voltage, overpotential, and the spacing-membrane-spacing series resistor model. Note that the large pore diameter, 350 μm thick membrane resistance and the spacing resistance are on the same order (both order

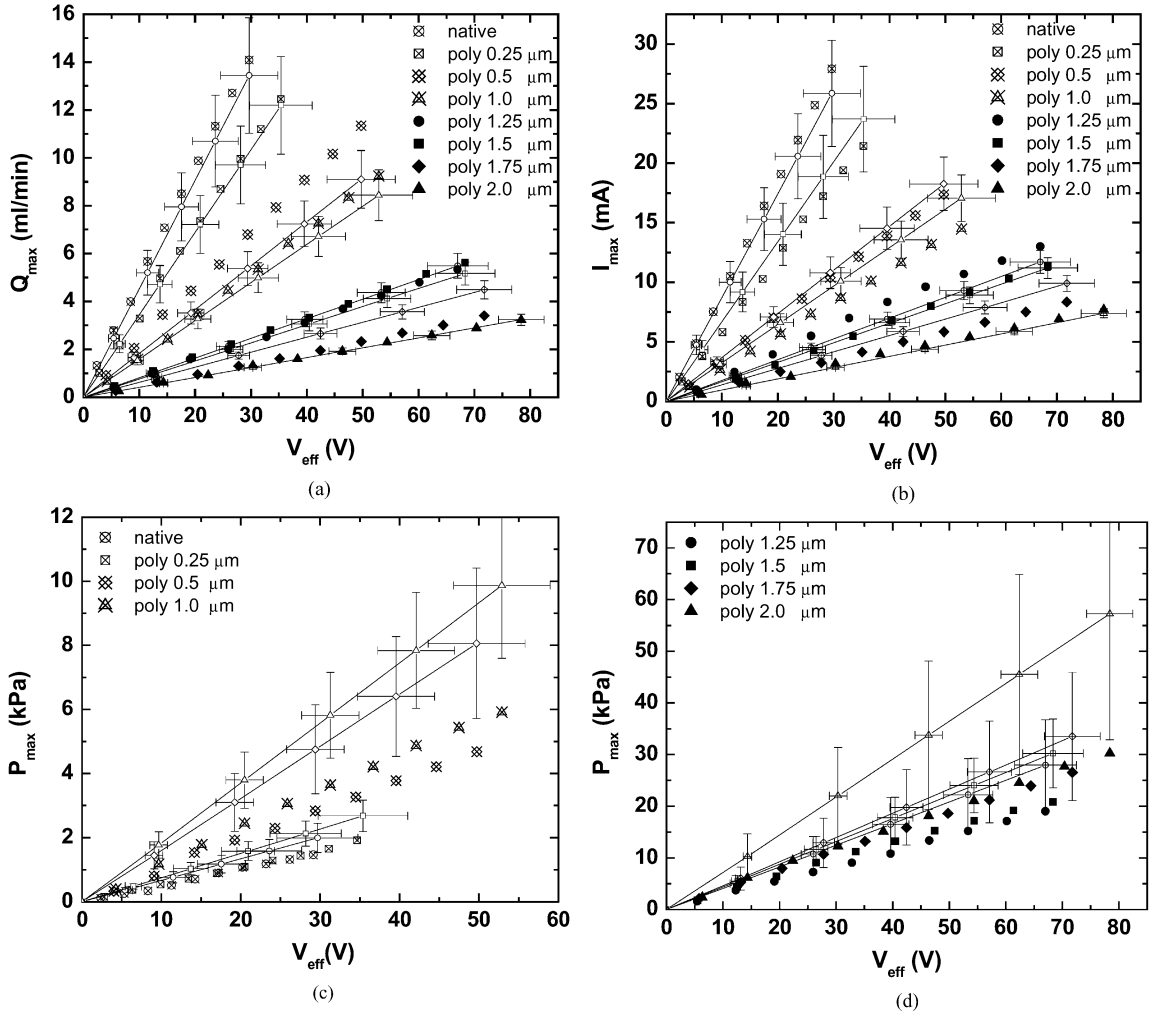

Fig. 8. Measured values of maximum flow rate (a), current (b), and pressure (c) and (d) (shaded symbols) versus effective voltage for porous silicon EO pumps with various thicknesses of polysilicon deposition and 0.25 μm thick SiO_2 surface layers. Shown together with the data are model predictions (solid lines labeled with open symbols). Model predictions are given by $Q_{\max} = -\psi A \varepsilon \zeta V_{\text{eff}} f/(\mu L)$, $I_{\max} = \psi A \sigma V_{\text{eff}} f/(Lg)$, and $P_{\max} = -8\varepsilon\zeta V_{\text{eff}} f/a^2$, a measured typical value of -104 mV for zeta potential, the porosity and pore radii obtained from image analysis (Table I), and the effective voltage estimated from the electrode coupling parameters.

1 000 Ohm); while the membrane resistance of other membranes is 1 to 7 times larger than the spacing resistance. The electrode spacing resistance and overpotential reduced the effective potential difference along the pump to a range from 2 to 78 V from the applied potential difference range from 10 to 100 V.

The membranes of the devices shown in Fig. 8 had an equal number density of pores, and so the largest flow rate pump was the membrane with native SiO_2, as expected. The thickness of the native oxide was less than 20 Å. The maximum flow rate per unit applied voltage and unit area of this native-oxide sample was 0.13 ml/min/cm^2/V. This figure of merit is five times larger than previously demonstrated silica-based frit EO pumps [15]. The maximum flow rate capacity per power consumption is 20 ml/min/W, four times higher than that of the silica-based frit EO pump. The highest measured pressure per unit applied voltage was 300 Pa/V, achieved by the membrane with the smallest pores. The model shows very good agreement with measured values of current and flow rate for all of the samples. However, the model overpredicts the pressure capacity by 85% for the smallest pore radius and less than 60% for all the others.

TABLE II
WORKING ELECTROLYTES USED IN EXPERIMENTS pH = 9.2

Molar concentration of $Na_2B_4O_7$ (mM based on Na^+)	Conductivity (S/m)
0.2	1.61e-3
0.6	5.09e-3
1.0	81.1e-3
2.0	1.62e-2
3.0	2.30e-2
4.0	3.02e-2
5.0	3.80e-2

The discrepancy in pressure prediction is most likely due to three major factors. First, the zeta potential values used for the prediction were obtained from measurements of maximum flow rate and current, both obtained at low pressure/high flow conditions (using (7)). However, the electrolyte's buffering strength is probably overcome at the low-flow-rate condition required to obtain maximum pressure. This results in locally decreased zeta potential values, and predictions that are biased toward higher-than-expected pressure performance. This issue is discussed in detail below and supporting evidence shown in

Fig. 10. We estimate this issue alone accounts for a pressure overprediction of 45%. The second important source of uncertainty in predicted pressure is the fact that the simple model uses a single effective pore diameter, while the actual device has a distribution of pore diameters. Yao [27] discusses the effects of polydiperse pore distributions on pump performance and presents models that account for wide pore diameter distributions. The third source of uncertainty is in the measurement of average pore diameter for each sample. The smallest pores are the most difficult to characterize via image analysis and have geometries that deviate greatly from that of straight, cylindrical pores. In Table I, we summarize pore radii estimates obtained from $Q_{\max}/P_{\max}$ measurements with those obtained from image analysis. The pore radius estimates from $Q_{\max}/P_{\max}$ followed the same trends as the SEM image analysis results but were about 10% larger, a discrepancy probably due to the effects of image noise (note that a 10% underestimation of pore diameter alone results in a 21% overestimation of pressure). The contributions to the discrepancy of the theory and experiments can be summarized as follows:

1) the empirically determined zeta potentials are biased toward high-pressure conditions;
2) the model prediction uses a simple monodiperse distribution of pore diameters instead of the actual polydisperse pore distribution;
3) the SEM image analysis slightly underestimates the pore diameters due to image noise.

We can also calculate the flow rate per power for the porous silicon pumps. From the data of Figs. 8(a) and (b), $Q/(I*V_{\rm app})$ varies between 12 to 20 ml/min/W for the small and large pore pumps, respectively. The thermodynamic efficiency varies between 0.003% to 0.05% for the small and large pore pumps, respectively. As expected for these relatively large pore diameter pumps, $Q/(I*V_{\rm app})$ is roughly four times higher than typical glass pumps [15], while the thermodynamic efficiency is 4 to 67 times lower than typical pumps [15] (assuming equivalent values of electrode spacing and electrolyte conductivity).

Fig. 9(a) shows the raw data for the characterization of pump performance with various thicknesses of polysilicon depositions and SiO_2 coatings at 25 V applied voltage. The flow rate and pressure were measured at approximately steady state conditions (after more than 1 minute of run time per point). Fig. 9(b) shows a normalized version of the same data as Fig. 9(a). In this second figure, flow rate was nondimensionalized by $Q_{\max}$ and the pressure by $P_{\max}$, using the parameters discussed above to calculate $Q_{\max}$ and $P_{\max}$ for each sample respectively. Shown with the data is a linear regression fit (dashed line) with 95% confidence interval error bars obtained from a propagation of error analysis [28] predicting errors in normalized pressure and flow rate from uncertainties in each of the independent parameters. Important contributions to overall uncertainty include uncertainties associated with the prediction of effective voltage (associated with small variations of electrode spacing across experiments); uncertainty in pore diameter associated with the standard-deviation width of measured pore distributions (Table I). The respective effective voltages for these experiments varied from 7 V to 18 V for membranes,

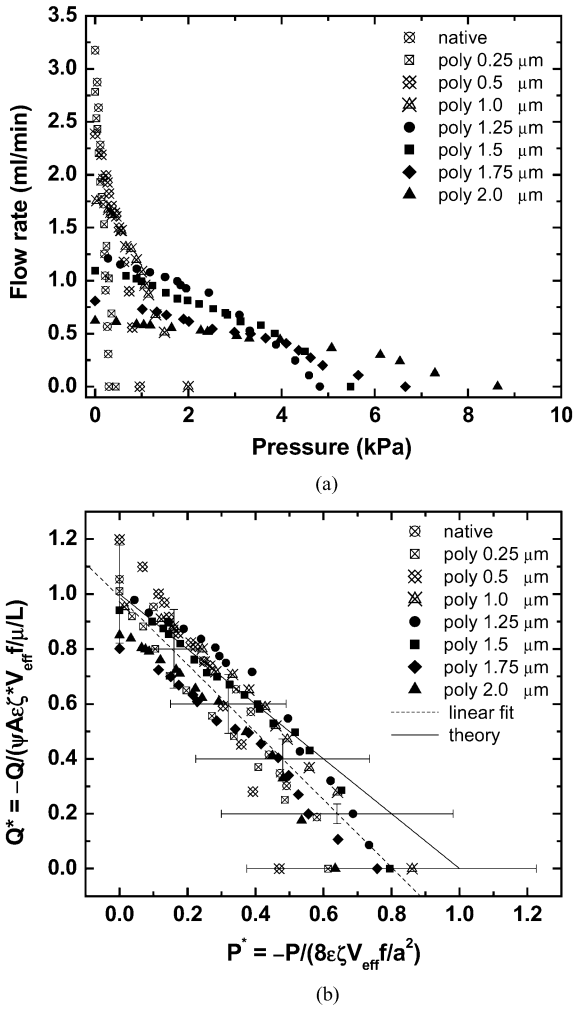

Fig. 9. (a) Flow rate versus backpressure for porous silicon EO pumps with various thicknesses of polysilicon deposition and 0.25 μm thick SiO_2 surface layer at an applied voltage of 25 V. (b) Normalized flow rate versus pressure. The flow rate and pressure are nondimensionalized by $Q_{\max} = -\psi A\varepsilon\zeta V_{\rm eff} f/(\mu L)$ and $P_{\max} = -8\varepsilon\zeta V_{\rm eff} f/a^2$, using a nominal zeta potential value of -104 mV, porosity and pore radius values from image analysis (Table I), and the effective voltage estimated from the electrode coupling parameters. Shown together with the data are a linear fit (dashed line) with error bars determined from an error propagation analysis. Also shown is a theoretical model prediction (solid line).

with lower effective voltages associated with larger pores. As in the measurements of Fig. 8, the largest contributors to uncertainty in flow rate are effective voltage and zeta potential uncertainties. The largest contributors to pressure uncertainty are uncertainties in characterization of the effective pore diameter (note that pressure varies as the inverse of the square of pore diameter).

Under the normalization of Fig. 9, the data across eight samples with eight different pore diameters should approximately collapse onto a single line of the form $Q^* = 1 - P^*$, where $Q^* = Q/Q_{\max}$ and $P^* = P/P_{\max}$. This expected global characterization curve is shown as a solid line in the figure. This theoretical line has approximately the ordinance-intercept as the regression fit to the data. However, the regression fit shows a markedly lower intercept (i.e., a lower maximum pressure than predicted). We attribute this latter effect to poor performance of

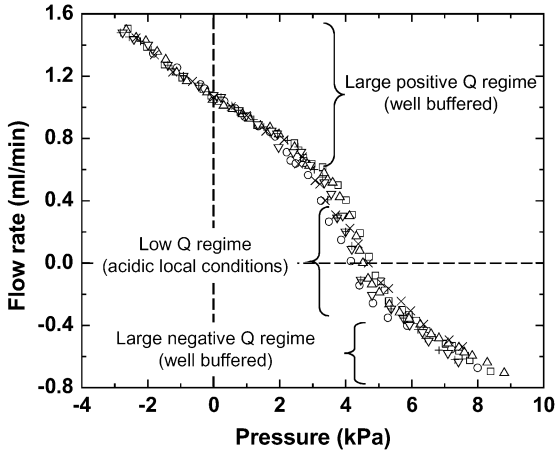

Fig. 10. Flow rate versus backpressure for a porous silicon pump with 1.25 μm polysilicon deposition and a 0.25-μm SiO_2 surface layer at applied voltage of 25 V. The backpressure data varied from favorable pressure differences to adverse pressure loads in excess of pump pressure capacity. Shown are data from six realizations demonstrating repeatability of the process.

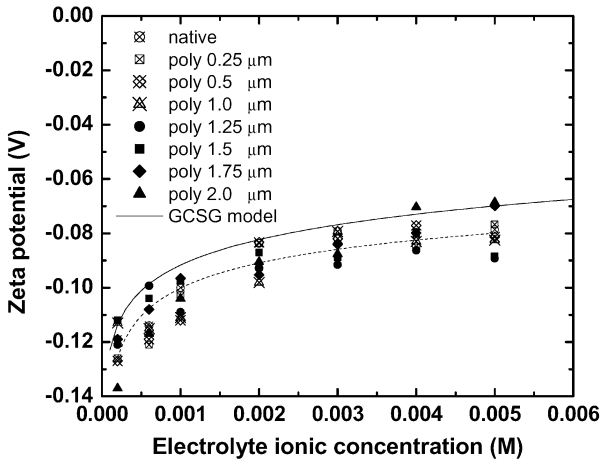

Fig. 11. Measured zeta potential as a function of molar concentration for sodium borate buffer. The molarity values are based on the molar concentration of sodium ions. Data are shown for eight porous silicon samples with various thicknesses of polysilicon deposition and SiO_2 coating surfaces. The dashed line is a fit for (10) with $c_0 = 1$ M, $\zeta_0 = -0.038$ V, and $\mathrm{N} = 0.14$. The solid line shows a prediction using a curve fit to the GCSG model for the KCl/silica model given by [15].

the buffer at low flow rate conditions, as discussed in the next section. Overall, the model is able to capture the major trends in the data to within estimated uncertainties.

C. Repeatability and pH Degradation

The extended pressure load capability of the experimental setup in Fig. 6(b) allows us to study the effects of pump flow rate on local pH conditions. For each porous silicon sample, we used this set up to measure flow rate versus pressure curves for at least a few realizations to sestablish repeatability. For a single sample, the flow rate-pressure curves were repeatable to within $\pm 11\%$ over six realizations. Measurements of extended pressure versus flow rate for the 1.25 μm polysilicon deposition pump at 25 V applied voltage are shown in Fig. 10 for six realizations of the experiment. At high flow conditions (above 0.4 ml/min and below -0.4 ml/min), pressure-flow rate slopes were linear and equivalent. The curves were linear throughout much of the flow rate and pressure range, as predicted by (1). However, both pressure and flow rate noticeably dropped to lower values at low flow conditions due to unfavorable changes in pH. We attribute this behavior at low net flow rates to nonuniform and unsteady pH fields associated with electrolysis of the buffer [29]. At low flow rate magnitudes, the buffer in the vicinity of the pumps is replenished at a low rate and electrolysis reactions can locally exceed the buffering capacity of the buffer. At this condition, pH values are compromised particularly in the anode region where pH tends to drop lower than the nominal amount [29]. These pH changes lower pump zeta potential and result in diminished EO pump performance. The effects of the pH degradation are significant. A simple linear extrapolation of the high flow rate performance of the pumps, results in a 45% overestimation of the maximum pressure capability of the pump (see discussion of Fig. 8(c) and (d) above).

For selected measurements, the pH of electrolyte in the vicinity of the pump was monitored using an eight-color universal pH indicator (Sigma-Aldrich, Allentown, PA). At low flow rate magnitude conditions (below about 0.4 ml/min), pH values of the electrolyte in the anode reservoir region decrease from 9 to below 8, over a 15 min period at an applied voltage of 25 V. The observations are consistent with the hypothesis that low flow rate EO pumps have unstable pH fields. This low-flow rate pH degradation has also been reported by Yao *et al.* [30] and Brask *et al.* [29].

pH gradients can adversely affect pump performance under low flow conditions. Buffer selection is therefore essential to the stable operation of any EO pump as zeta potential is a function of both pH and ion density [7]. We suggest electrolyte chemistry be chosen carefully as a tradeoff between thermodynamic efficiency (or flow rate per current performance) and operational stability. Ion selective membranes that separate the electrodes from the pumping media may be effective at mitigating electrolysis induced pH gradients [14], [26].

D. Zeta Potential Estimation

We estimated the zeta potential of porous silicon membranes by measuring both maximum flow rate and current using borate buffers with seven concentrations varying from 0.2 to 5 mM, as shown in Table II. We calculate zeta potential from (7) using the measured values of $Q_{\max}, I_{\max}$, and σ. Permittivity and viscosity are assumed constant, a good assumption in the current experiments which have negligible Joule heating effects. Values of g were calculated numerically for various pore radii and Debye lengths [20]. The working electrolytes for these zeta measurement experiments are given in Table II. Fig. 11 shows the trend of zeta potential versus electrolyte molar concentration of sodium borate buffer. Data are shown for eight porous silicon samples with various thicknesses of polysilicon deposition and SiO_2 coating surfaces. The solid line shows a prediction using the curve fit to the Gouy–Chapman–Stern–Grahame (GCSG) model for the KCl/silica [15]. The experimental results suggest that zeta potential has a power-law scaling with concentration of the form

$$\zeta = \zeta_o (c/c_o)^{-N} \tag{10}$$

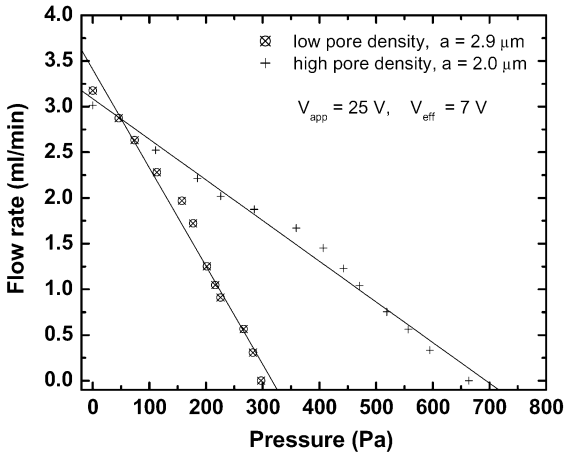

Fig. 12. Flow rate versus backpressure for low-pore density and high-pore density porous silicon EO pumps at 25 V applied voltage (Data for the low-pressure performance native-oxide sample are shown). The two porous silicon membranes have native SiO_2 surfaces with only 20 Å in thickness. The pore size and porosity values are listed in the first and last row of Table I. The two pumps show similar flow rate but the pressure capacity of the smaller-pore, high-pore density pump is 2.2 times greater than that of the low-pore density pump.

where ζ_o is the reference zeta potential for the reference electrolyte concentration, c_o. If we choose $c_o = 1$ M, a curve-fit of the experimental data points gives $\zeta_o = -0.038$ V and $N = 0.14$. In comparison, zeta potential measurements we have reported for borosilicate glass in contact with borate buffer [15] scale approximately as $c^{-0.3}$. Sadr *et al.* measured an EOF mobility scaling as $c^{-0.28}$ for sodium tetraborate buffer/fused silica [31]. For 1 mM (Na+) borate buffer, the average zeta potential is -104 ± 5 mV (uncertainty reflects 95% confidence intervals for distribution of eight measurements). This value is comparable to the zeta potential of -106 mV value for borosilicate glass operated with the same buffered electrolyte [15]. Because the charge sites on SiO_2 are invariably Si-OH, regardless of the silica type or deposition technique, thin SiO_2 layers perform much like bulk silica [22]. Assuming constant surface charge density, the dependence of ζ on ionic concentration (given constant temperature and dielectric constant) can be derived in the low- and high- ζ limits of the non linear Poisson–Boltzmann equation solution in the double layer. As summarized by Kirby *et al.* [22], the low-potential scaling $(\zeta \sim c^{-0.5})$ is generally applicable for silica at low pH (<3.5) or high ionic concentration $(>200$ mM). The high-potential scaling $(\zeta \sim \log c)$ is generally applicable for silica below 100 mM at $\mathrm{pH} > 6$ and below 10 mM at $\mathrm{pH} > 3.5$. From a pragmatic standpoint, the logarithmic scaling (similar to power law scaling) leads to a much more satisfactory match with the experimental results.

E. Porosity Optimization and Ultimate Limits on Thin Pumps

Feature dimensions of the porous silicon layout can be optimized to maximize both flow rate and pressure capacity. In general, increasing pore number density for a given pore diameter, results in higher (porosity and) flow rate while maintaining constant pressure capacity; but this also tends to structurally weaken the membrane. Alternately, higher number density can be coupled with decreasing pore diameter to obtain higher pressure for a given flow rate. We demonstrated the ability to achieve higher specific performance with experiments on a high number density sample. We obtained porous silicon membranes from Neah, Inc. with a hexagonal array of pores and a number density 2.2 times larger than the membranes described in Figs. 1 and 2 above. The final sample has pore diameters of about 2 μm, center-to-center distances of 5.5 μm, and an overall porosity of 0.42, as measured by image analysis of SEM images. Fig. 12 shows the flow rate-pressure curves for this high pore density porous silicon EO pump with native SiO_2 surfaces at applied 25 V. Data from a low pore density sample with native oxide surface is shown for comparison. The low pore density sample as an approximately equal porosity of 0.39, and so both samples show a similar maximum flow rate, as expected. However, the pore diameter of the high pore density membrane is 1.5 times smaller than that of the low pore density membrane, resulting in 2.2 times greater pressure as predicted by (5).

VIII. Conclusion

We have demonstrated EO pumping of large flow rate per unit voltage and area using porous silicon pumping media. Our porous silicon pumps can generate a maximum flow rate of 3.2 ml/min at 25 V applied voltage, with a compact pumping medium volume of 35 mm^3. The geometry and material of the pumping structures were characterized in the terms of pore size and porosity. Image analysis techniques were applied to optical micrographs and scanning electron micrographs to directly measure the pore number density, pore radius, and porosity. The experimental results compare well with our previously published theoretical model, which uses the measured values of pores size and porosity. The model prediction agrees very well with current and flow rate measurements, but typically overpredicts measured pressure capacity by about 60%. This discrepancy is probably due to the fact that zeta potential of low-flow-rate, high-pressure performance of the pumps is less than that of the well buffered, high-flow rate case. Other possible causes are that the model uses an effective pore diameter to approximate a pore diameter distribution, and that the image analysis slightly overpredicts pore diameter.

The repeatability and stability of the pump operation were addressed by extended pressure and flow rate measurement over six realizations. EO pump performance is compromised at low net flow conditions by the effects of electrolysis reactions on buffer pH. Electrolyte chemistry (in particular ion concentrations and mobilities) should be chosen as a tradeoff between pH stability and pumping efficiency. We measured the zeta potential for these porous silicon pumps with silicon oxide surfaces as -104 mV at pH 9 and ionic concentration of 1.0 mM (Na+). The measurements of zeta potential over a range of ionic concentrations suggest a power law scaling of zeta potential as a function of concentration, which is consistent with published data trends. Both flow rate and pressure performance of porous silicon membrane pumps can be optimized by increasing pore density.

Acknowledgment

The authors would like to thank Neah Power Systems for providing the porous silicon membranes.

REFERENCES

[1] L. Jiang, J. C. Mikkelsen, J.-M. Koo, D. Huber, S. Yao, L. Zhang, P. Zhou, J. G. Maveety, R. Prasher, J. G. Santiago, T. W. Kenny, and K. E. Goodson, "Closed-loop electroosmotic microchannel cooling system for VLSI circuits," *IEEE Trans. Compon. Packag. Technol.*, vol. 25, no. 3, pp. 347–355, 2002.

[2] P. K. Wong, T.-H. Wang, J. H. Deval, and C.-H. Ho, "Electrokinetics in micro devices for biotechnology applications," *IEEE/ASME Trans. Mech.*, vol. 9, pp. 366–376, 2004.

[3] T. E. McKnight, C. T. Culbertson, S. C. Jacobson, and J. M. Ramsey, "Electroosmotically induced hydraulic pumping with integrated electrodes on microfluidic devices," *Anal. Chem.*, vol. 73, pp. 4045–4049, 2001.

[4] D. J. Laser and J. G. Santiago, "A review of micropumps," *J. Micromech. Microeng.*, vol. 14, no. #6, pp. R35–64, 2004.

[5] V. Proetorius, B. J. Hopkins, and J. D. Schieke, "Electroosmosis: a new concept for high-speed liquid chromatography," *J. Chromatogr. A*, vol. 99, pp. 23–30, 1974.

[6] F. Theeuwes, "Elementary osmotic pump," *J. Pharm. Sci.*, vol. 64, no. 12, pp. 1987–1991, 1975.

[7] W. Gan, L. Yang, Y. He, R. Zeng, M. L. Cervera, and M. Guardia de la, "Mechanism of porous core electroosmtic pump flow infection system and its application to determination of chromium (VI) in waste-water," *Talanta*, vol. 51, pp. 667–675, 2000.

[8] P. H. Paul and D. J. Rakestraw, "Electrokinetic High Pressure Hydraulic System," U.S. Patent 6 019 882, 2000.

[9] S. Zeng, C. H. Chen, J. G. Santiago, J. Chen, R. N. Zare, J. A. Tripp, F. Svec, and J. Fréchet, "Electroosmotic flow pumps with polymer frits," *Sens. Actuators B, Chem.*, vol. B82, no. 2–3, pp. 209–212, 2001.

[10] S. Zeng, C. H. Chen, J. C. Mikkelsen, and J. G. Santiago, "Fabrication and characterization of electroosmotic micropumps," *Sens. Actuators B, Chem.*, vol. B79, no. 2–3, pp. 107–114, 2001.

[11] S. Yao, D. Huber, J. C. Mikkelsen, and J. G. Santiago, "A large flowrate electroosmotic pump with micron pores," in *Proc. Int. Mech. Eng. Congr. Expo., Sixth Microfluid. Symp.*, New York, NY, 2001.

[12] C. H. Chen and J. G. Santiago, "A planar electroosmotic micropump," *J. Microelectromech. Syst.*, vol. 11, no. 6, pp. 672–683, 2002.

[13] D. J. Laser, S. Yao, C. H. Chen, J. C. Mikkelsen, K. E. Goodson, J. G. Santiago, and T. W. Kenny, "A low-voltage silicon micromachined parallel-plate electrokinetic pump," in *Proc. 11th Int. Conf. Solid-State Sens. Actuators (Transducers'01)*, Munich, Germany, 2001.

[14] Y. Takamura, H. Onoda, H. Inokuchi, S. Adachi, A. Oki, and Y. Horiike, "Low-voltage electroosmosis pump for stand alone microfluidics devices," *Electrophoresis*, vol. 24, pp. 185–192, 2003.

[15] S. Yao, D. E. Hertzog, S. Zeng, J. C. Mikkelsen, and J. G. Santiago, "Porous glass electroosmotic pumps: design and experiments," *J. Colloid Interface Sci.*, vol. 268, pp. 143–153, 2003.

[16] H. Föll, M. Christophersen, J. Carstensen, and G. Hasse, "Formation and application of porous silicon," *Mater. Sci. Eng. Rev.*, vol. 39, pp. 93–141, 2002.

[17] L. T. Canham, "Silicon quantum wire array fabrication by electrochemical and chemical dissolution of wafers," *Appl. Phys. Lett.*, vol. 57, pp. 1046–1048, 1990.

[18] H. Presting, J. Konle, V. Starkov, A. Vyatkin, and U. Konig, "Porous silicon for micro-sized fuel cell reformer units," *Mater. Sci. Eng. B*, vol. 108, no. 1–2, pp. 162–165, 2004.

[19] S. Ottow, V. Lehmann, and H. Föll, "Development of three-dimensional microstructure processing using macroporous n-type silicon," *Appl. Phys. A*, vol. 63, pp. 153–159, 1996.

[20] S. Yao and J. G. Santiago, "Porous glass electroosmotic pumps: Theory," *Journal of Colloid Interface Science*, vol. 268, pp. 133–142, 2003.

[21] R. J. Hunter, *Zeta Potential in Colloidal Science: Principles and Applications*. London, U.K.: Academic, 1981.

[22] B. J. Kirby and E. F. Hasselbrink Jr., "Zeta potential of microfluidic substrates: 1. Theory, experimental techniques, and effects on separations," *Electrophoresis*, vol. 25, no. 2, pp. 187–202, 2004.

[23] ——, "Zeta potential of microfluidic substrates: 2. Data for polymers," *Electrophoresis*, vol. 25, no. 2, pp. 203–213, 2004.

[24] D. S. Reichmuth, G. S. Chirica, and B. J. Kirby, "Increasing the performance of high-pressure, high-efficiency electrokinetic micropumps using zwitterionic solute additives," *Sens. Actuators B, Chem.*, vol. B92, no. #1–2, pp. 37–43, 2003.

[25] R. C. Gonzalez and R. E. Woods, *Digital Image Processing*, 2nd ed. Upper Saddle River, NJ: Prentice Hall, 2002.

[26] D. J. Harrison, P. G. Glavina, and A. Manz, "Toward miniaturized electrophoresis and chemical analysis systems on silicon: An alternative to chemical sensors," *Sens. Actuators B, Chem.*, vol. B10, pp. 107–116, 1993.

[27] S. Yao, "Theory, Design, and Demonstration of Electroosmotic Pump Technologies," Ph.D. Thesis, Stanford University, 2005.

[28] H. W. Coleman and W. G. Steele, *Uncertainty Analysis*. Boca Raton, FL: CRC Press, Inc., 1998, ch. 39. CRC Handbook of Fluid Dynamics.

[29] A. Brask, H. Bruus, and J. P. Kutter, "Long-term stability for frit-based EO pumps under varying load conditions using ion exchange mambranes with controlled diffusion layer widths," in *Proc. μTAS 2004 8th Int. Conf. Mini. Syst. Chem. Life Sci.*, Malmö, Sweden, 2004.

[30] S. Yao, A. M. Myers, J. D. Posner, and J. G. Santiago, "Electroosmotic pumps fabricated from porous silicon membranes," in *Proc. Int. Mech. Eng. Conf. Expo.*, Anaheim, CA, 2004.

[31] R. Sadr, M. Yoda, Z. Zheng, and A. T. Conlisk, "An experimental study of electroosmotic flow in rectangular microchannels," *J. Fluid Mech.*, vol. 506, pp. 357–367, 2004.

Shuhuai Yao received the B.S. degree in engineering mechanics from Tsinghua University, Beijing, China, in 2000 and the M.S. and the Ph.D. degrees in mechanical engineering from Stanford University, Stanford, CA, in 2001 and 2005, respectively.

Her graduate research focused on the development of microfluidic and MEMS devices for electronic cooling systems and bioanalytical applications. She has published the theoretical and experimental research work of miniaturized, high-flow rate electroosmotic micropumps and the integration of a recombination system for control of electrolytic gases. Currently, she is a Postdoctoral Fellow in Lawrence Livermore National Labs, where she is engaged in the development of ultrafast microfluidic mixers for study of protein folding reactions.

Alan M. Myers received the B.S. degree in metallurgical engineering from the University of Illinois at Chicago in 1984 and the Ph.D. degree in materials science from the University of Illinois at Urbana Champaign in 1991.

He joined the Portland Technology Development Division of Intel in 1992 and is currently a member of the External Programs division of Intel. He has published approximately 20 archival journal and conference articles. He currently holds 20 patents with an additional 18 patent applications pending with the United States patent office. He has spent the past three years as an Intel Researcher in Residence at Stanford University, Stanford, CA, investigating electroosmotic pumps and microchannel cooling. He is currently working on developing extreme ultraviolet lithography for high-volume manufacturing operations.

Jonathan D. Posner received the M.S. and Ph.D. degrees in mechanical engineering at the University of California, Irvine, in 1998 and 2001, respectively.

In addition, he spent 18 months as a fellowship student at the von Karman Institute for Fluid Mechanics in Rhode Saint Genese, Belgium. As a Research Scientist at Neophotonics Corporation he developed an aerosol based, laser pyrolysis nanoparticle reactor for optical films, and fuel cell electrolytes. He also spent two years as a Postdoctoral Fellow at Stanford University, Stanford, CA, in the Mechanical Engineering Department. He is currently an Assistant Professor at Arizona State University in the Department of Mechanical and Aerospace engineering. His interests include microscale transport phenomena, fluid dynamics, electrokinetics, and optical diagnostics as they apply to the physics and design of micro/nanofluidic bioanalytical and energetic devices. Applications of his research include: novel bioassay functionality, personalized medicine (genome/proteome specific therapy), precision biology, real-time environmental monitoring, drug delivery, and fuel cells.

Dr. Posner was honored for his Excellence in Experimental Research by the von Karman Institute for Fluid Dynamics and his work has appeared on the cover of *Applied Optics* and the *Journal of Microfluidics and Nanofluidics*.

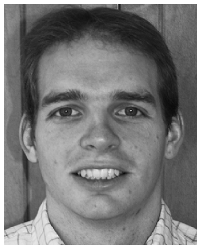

Klint A. Rose received the B.S. and M.S. degrees in mechanical engineering from the Massachusetts Institute of Technology (MIT), Cambridge, in 2001 and 2002, respectively. Currently, he is working toward the Ph.D. degree in mechanical engineering from Stanford University, Stanford, CA. His work in the Stanford Microfluidics Laboratory focuses on the manipulation of micron-scale rod-like particles for biological applications.

He joined Lawrence Livermore National Laboratory (LLNL) in 2002, where he is presently working on the autonomous pathogen detection system (APDS). Past projects at LLNL include microfluidic systems for droplet manipulation and polymer-based hybrid integrated microsystems.

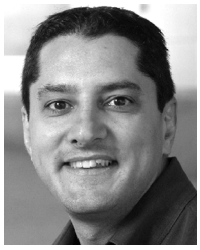

Juan G. Santiago (M'99) received the Ph.D. degree in mechanical engineering from the University of Illinois at Urbana-Champaign (UIUC).

At UIUC, he received four fellowships as a doctoral candidate (including fellowships from NSF and Exxon Corp.), and a UIUC Teaching Fellow Award. He was a Senior Member of the Technical Staff at the Aerospace Corporation from 1995 to 1997, where his work included the development of flow diagnostics for micronozzles. Prof. Santiago received a Ford Foundation Postodoctoral Fellowship (1997), and worked as a Research Scientist at UIUC's Beckman Institute from 1997 to 1998. He is an Associate Professor in the Mechanical Engineering Department at Stanford University, Stanford, CA, where he specializes in microscale fluid mechanics, microscale optical flow diagnostics, and microfluidic system design. He is the Director of the Stanford Microfluidics Laboratory. His research includes the investigation of transport phenomena and optimization of microsystems for pumping liquids, electrophoretic injections and separations, sample concentration methods, and rapid micromixing processes. The applications of this work include microfabricated bioanalytical systems for genetic analysis and drug discovery.

Dr. Santiago has received a Frederick Emmons Terman Fellowship 1998–2001), won the National Inventor's Hall of Fame Collegiate Inventors Competition (2001), and was awarded a National Science Foundation PECASE Award (2003–2008). He is a member of the American Society of Mechanical Engineers (ASME).